Available online at www.sciencedirect.com
SCIENCE DIRECT®
Journal of Solid State Chemistry 177 (2004) 6–16
JOURNAL OF SOLID STATE CHEMISTRY
http://elsevier.com/locate/jssc

Real structure of $KInS_2$ polytypes

L. Kienle,[a,*] V. Duppel,[a] A. Simon,[a] M. Schlosser,[b] and O. Jarchow[c]

[a] *Max-Planck Institut für Festkörperforschung, Heisenbergstr. 1, 70569 Stuttgart, Germany*
[b] *Universität Siegen, Adolf Reichweinstr., 57068 Siegen, Germany*
[c] *Mineralogisch-Petrographisches Institut, Universität Hamburg, Grindelallee 48, 20146 Hamburg, Germany*

Received 3 February 2003; received in revised form 9 April 2003; accepted 25 April 2003

Abstract

$KInS_2$ crystallizes in a two dimensionally ordered structure, which is related to the $TlGaSe_2$-type structure. High-resolution transmission electron microscopy (HRTEM) and the analysis of diffuse scattering give evidence for defined shifts between ordered layers, which establish a lamellar nanostructure. The different arrangements of the lamellas, designated as A and B are fully compatible with the pseudosymmetry of $KInS_2$. Consequently no misfit of the real structure can be observed by HRTEM. Only in rare cases the arrangement of the layers is at least partially ordered within extended domains and the diffuse scattering narrows into Bragg reflections. Two different strategies for the simulation of the diffuse scattering are presented. Besides the approximation of the diffuse scattering by Bragg intensities which are calculated on the basis of an ordered supercell, the diffuse scattering can also be simulated in dependence of the probability of AB or BA neighbors.

Keywords: High-resolution transmission electron microscopy; Polytypic structures; Diffuse scattering; Image simulation

1. Introduction

Many ternary compounds of general formula AMX_2 (A = Li, Na, K, Rb, Cs, Tl; M = Al, Ga, In; X = S, Se, Te) crystallize in the $TlGaSe_2$-type structure [1,2]. Besides semiconducting and ferroelectric properties (e. g. for $TlGaSe_2$ and $TlInS_2$, [3]) some of these compounds exhibit interesting peculiarities like pressure transformations [4] and disorder in the real structure [1]. The latter in combination with several types of twinning [5,6] makes an unambiguous determination of the structure difficult. For instance, the structures of $KMSe_2$ (M = Al, Ga, In), [7] were first described with supercells of tetragonal symmetry, while in the meantime an ordered model of the structures (space group $C2/c$) is generically accepted for many different compounds. In particular, for $KInS_2$ several publications confirm the close relation to the monoclinic structure of $TlGaSe_2$ (e.g., Refs. [8,9]).

An important feature of the structure are M_4X_{10} units which consist of four centered MX_4 tetrahedra. The M_4X_{10} units are connected via common corners into layers. There are two adjacent layers aligned parallel to (001) and perpendicular to [114] per unit cell and every eighth layer exactly coincides. Consecutive layers are connected via A^+ ions only, which are located in the centers of X_6 trigonal prisms. Hence, the interconnection of the layers is weak and the formation of stacking faults is facilitated. The disorder leads to remarkable anomalies in structure refinements of X-ray data, in particular to an elongation of the ellipsoids along [110] for those X-atoms, which are located close to the fault plane.

The stacking faults cause diffuse streaks in the diffraction patterns, which are aligned along c^*. X-ray diffraction (XRD) experiments on the paraelectric phase of $TlGaSe_2$ [10] gave first quantitative insights into the density of the stacking faults. The result is a model of the real structure with one stacking fault occurring approximately in every fourth plane.

A related disorder phenomenon is observed in the real structure of the orange modification of HgI_2 [11,12]. The motifs of the structure are Hg_4I_{10} units connected into layers. These are topologically equivalent to the layers in the $TlGaSe_2$-type structure. However, the arrangement of adjacent layers differs remarkably. Referring to the tetragonal structure of the ordered red modification of

*Corresponding author. Fax: +49-0711-689-1091.
E-mail address: l.kienle@fkf.mpg.de (L. Kienle).

0022-4596/03/$ - see front matter © 2003 Published by Elsevier Inc.
doi:10.1016/S0022-4596(03)00244-5

HgI_2, the different stackings in the polytypic structures are defined by the shift vectors: $s_1 = (1/2)a$ (or b) and $s_2 = 1/2(a+b)$. These shifts lead to a concept involving two supercells as units of the real structure. The first one is characterized by a four-layer structure (for s_1) and the second one by a two-layer structure (for s_2). The qualitative interpretation of the diffuse scattering indicates a mixture of domains with the four- and two-layer structure, besides more complex polytypes.

The great variety of crystal defects which occur in the real structure of compounds crystallizing in the $TlGaSe_2$-type structure serves as the basis of our interest for high-resolution transmission electron microscopy (HRTEM) studies.

2. Experimental

2.1. Preparation

Colorless transparent single crystals of $KInS_2$ have been prepared by heating stoichiometric mixtures of the elements up to 1273 K for 3 h in evacuated dry silica ampoules. The ampoules were quenched in ice water and the raw product was homogenized under inert atmosphere (argon) and annealed at 1123 K for 14 days.

2.2. Electron microscopy

Selected crystals of $KInS_2$[1] with sizes of several microns were crushed in an agate mortar and suspended in *n*-butanol. A perforated carbon/copper net was covered with the suspension, leaving wedge shaped crystallites in random orientations after drying. HRTEM, and selected area electron diffraction, SAED, were performed with a Philips CM30/ST (for basic parameters see Table 1).

The SAED patterns were obtained using a diaphragm, which limited the diffraction to a selected area of 2500 Å in diameter. Computer simulations of kinematical electron diffraction patterns and HRTEM images (multislice formalism) were calculated with the EMS program package [13]. The structural parameters of $KInS_2$ given by Eisenmann et al. [9] (space group: $C2/c$, $a = 11.003(5)$Å, $b = 10.995(5)$Å, $c = 15.021(6)$Å, $\beta = 100.60(6)$) served as a basis for all simulations and indexations. HRTEM images and SAED patterns were registered with a Slow Scan CCD Camera or a Multiscan CCD Camera. The software Digital Micrograph 3.4 (Gatan) was used for processing the high-resolution images. In order to reduce the small amount of noise resulting from a thin amorphous surface layer on the crystals, all HRTEM images were filtered after Fourier transformation by using a suitable band-pass mask. Great care was taken to avoid loss of essential information of the defect structure by image processing.

[1] In a second series of observations bulk material was selected for HRTEM. The results were essentially the same as for the observations of the single crystals.

Table 1
Basic parameters for HRTEM

Voltage	300 kV
Cathode	LaB_6
Spherical aberration constant (C_S)	1.15 mm
Maximum point resolution (300 kV)	1.9 Å
Spread of defocus	70 Å
Illumination semiangle	1.2 mrad
Tilting maximum (double tilt holder)	$\pm 25°$

Table 2
Summary of experimental details for the $KInS_2$ X-ray data collection

Radiation	Mo$K\alpha$, $\lambda = 0.71073$ Å
Monochromator	Graphite
Temperature	295 K
φ movement mode	Oscillation
φ range, $\Delta\varphi$	$-0.1° \leqslant \varphi \leqslant 219.9°, 0.5°$
$\theta_{min.}, \theta_{max.}$	2.3°, 30.45°
Image plate distance	50 mm
Irradiation time/image	6 min

2.3. X-ray diffraction

Crystals of suitable sizes for X-ray investigations were separated from the bulk product. The crystals were fixed on top of glass capillaries and mounted on a STOE IPDS I diffractometer; experimental details are summarized in Table 2. The measured data were analyzed with the STOE IPDS program package [14]. The programs INDEX and CELL were used to index the lattice and to obtain the orientation matrix. Undistorted views of layers in reciprocal space were calculated with the program SPACE.

3. Results

3.1. HRTEM

The crystals of $KInS_2$ selected for HRTEM exhibit features in their morphology which are frequently observed in compounds crystallizing in polytypic structures. All crystals consist of several very thin plates, which are shifted relative to each other, leading to the formation of steps on the crystal surface. The edge of the crystallite depicted in the bright field image of Fig. 1 was aligned with the zone axis [001] parallel to the electron beam. The thin plates are clearly separated at the thin edge of the crystal, however, they are grown together without any misfit. Therefore, SAED patterns indicate no significant splitting of the reflections $h\,k\,0$,

but strong fluctuations of their intensities due to double diffraction.

The disorder in the real structure is obvious from X-ray and electron diffraction patterns showing diffuse streaks at positions $h\,h\,l$ with $h = 2n + 1$. The diffuse streaks are aligned parallel to c^* (see Fig. 2a). When the examined crystallite is tilted perpendicular to c^*, the diffuse streaks of, e.g., zone axis pattern [110] disappear, as one would expect in the case of diffuse rods aligned parallel to c^* in reciprocal space. The shape of the diffuse scattering gives clear evidence for the existence of ordered layers parallel to (001) in the real structure of $KInS_2$. The intensity distribution of sharp reflections and diffuse maxima is a typical indication of a polytypic structure in class I [15], i.e., the real structure contains layers which are related by defined shift vectors. No significant diffuse intensities for the Bragg reflections $h\,h\,l$ with $h = 2n$ were observed, a fact which is connected with the superposition structure (SPS) of $KInS_2$. Reflections H, $K = (h,k)/2$ and $L = l$ are sharp and correspond with the orthorhombic SPS which is characterized by the lattice A, $B = (a,b)/2$, $C = 2c \sin\beta$ and the space group *Fddd*. An alternative description of the SPS is possible in the tetragonal system (space group $F4_1/ddm$). The statistical application of the stacking vectors $(A,B)/2$ leads to the 1D disordered structure, visible in diffuse streaks at positions h, $k = 2n + 1$. Of course, the stacking vectors can also be applied to construct ordered layer sequences. It can be shown [15] that all of these ordered domains are characterized by a C-centering of the structure. The symmetry of these ordered sequences are in subgroup relationship to the orthorhombic (or tetragonal) SPS. The most important case are domains with the symmetry $C2/c$ and the lattice a, b, c and $\beta \approx 100.8°$. This structure is identical with the ordered structure reported by Eisenmann [9].

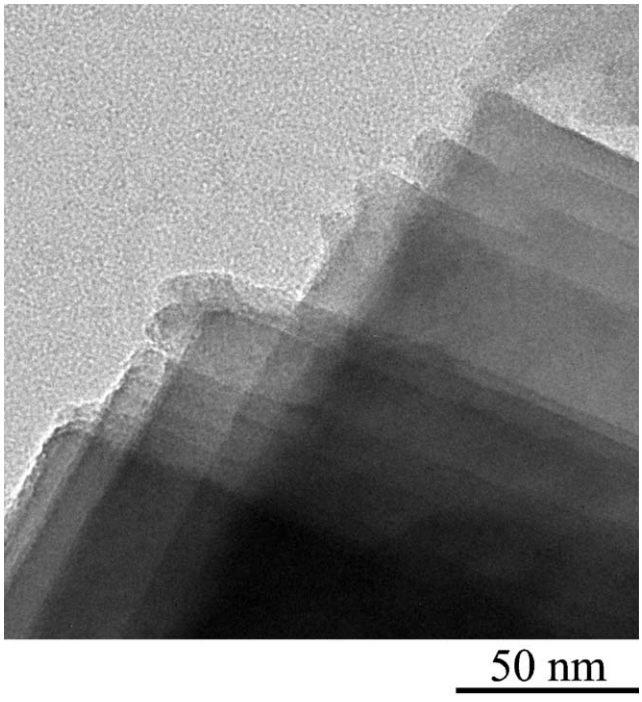

Fig. 1. TEM bright field image of one crystallite of $KInS_2$ aligned in the zone axis orientation [001].

SAED patterns of different crystal fragments show remarkable fluctuations in their diffuse intensity. Comparable fluctuations are also observed in diffraction patterns taken on the same crystallite but shifting the position of the SAED aperture, see Figs. 2a and b. The local extent of disorder is indicated by more (Fig. 2a) or less (Fig. 2b) extended streaks along c^* in electron diffraction patterns as verified by parallel HRTEM investigations.

HRTEM was performed in order to analyze the atomic structure at fault planes between the ordered

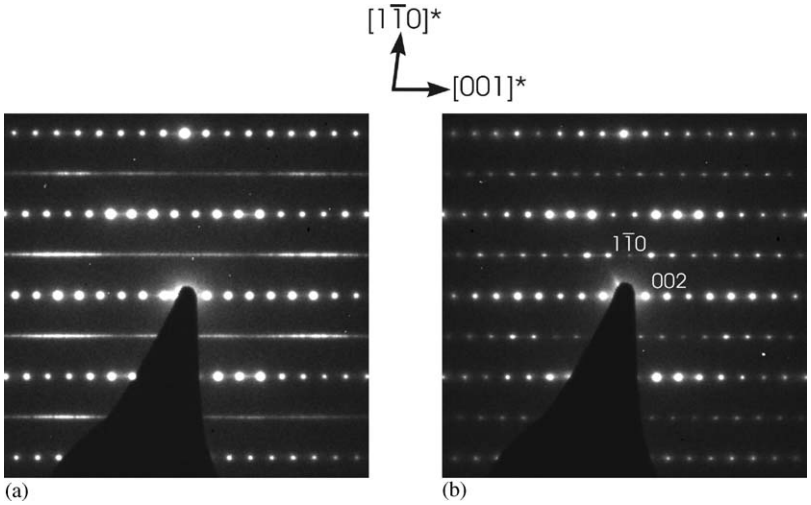

Fig. 2. SAED patterns (zone axis [110]) taken on different regions of *one* crystallite.

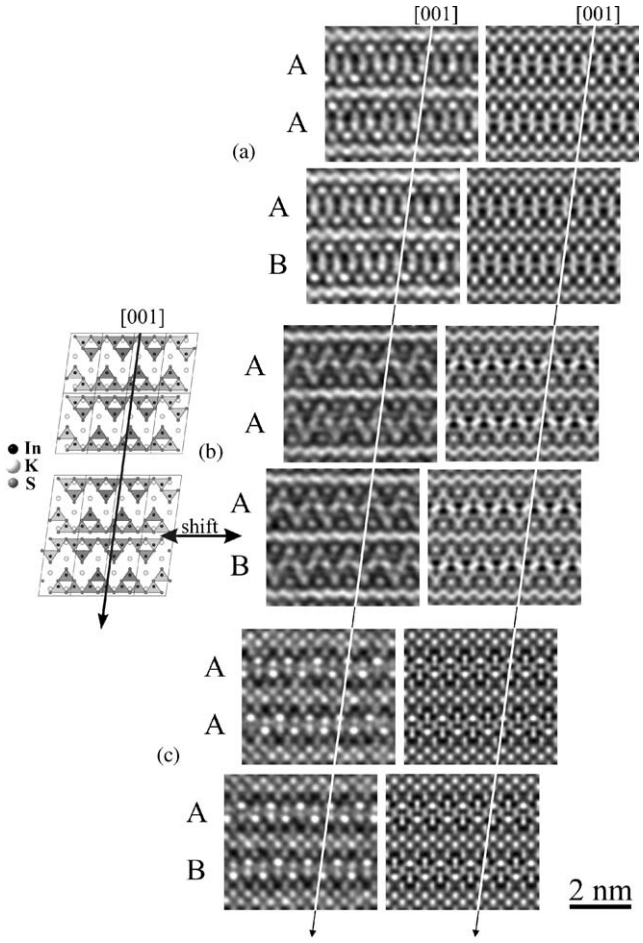

Fig. 3. Right: series of HRTEM micrographs with variable defocus (a) $\Delta f = -50$ nm, (b) $\Delta f = -60$ nm, (c) $\Delta f = -80$ nm taken on one crystallite together with image simulations (thickness: 3.1 nm). Left: structure models for the simulations in polyhedral representation.

layers. The micrographs shown in Figs. 3a–c (zone axis [110], variable defocus) were recorded in different thin regions of *one* crystallite. The experimental images are depicted on the left, the simulated ones on the right side. The micrographs of Fig. 3b were taken near Scherzer defocus optimum ($\Delta f = -60$ nm). Assuming the weak phase approximation the contrasts correlate with the projected potential of the crystal. Hence the positions of the atoms are displayed in black and the cavities of the structure in white. The peculiar white zigzag patterns in the micrographs of Fig. 3b correlate with the cavities between two adjacent layers, see the polyhedral representation on the left side of Fig. 3b. These two layers form an essential unit of the real structure, i.e., a lamella of $nx \times ny \times z$ unit cells referring to the monoclinic $TlGaSe_2$-type structure. The presented cut-outs of high-resolution images contain two lamellas designated as A or B with respect to their relative position along [001], see inscriptions in Fig. 3. Consecutive lamellas exhibit two different arrangements. The zigzag patterns within the centers of consecutive lamellas coincide along [001] for a sequence AA, but not for AB. In order to interpret the latter image the structural parameters of $KInS_2$ were transformed into space group $P1$ with a doubling of the original monoclinic c-axis. The resulting structure model consists of two lamellas per unit cell. The plane between the second and third layer offers the possibility to simulate a stacking fault by shifting the third layer, see the arrow on the left side of Fig. 3b. The shift between the lamellas is defined by the vector $s_1 = (1/4)a - (1/4)b$. No misfit at the boundary of lamella A and B was observed by HRTEM. This is confirmed by the convincing agreement between simulated images and micrographs taken with variable defocus. The micrographs presented in Fig. 3 clearly indicate the shift between the lamellas for the sequence AB. However, the atomic structure at the boundary of consecutive lamellas is identical for the sequences AA and AB within the resolution of the electron microscope. This is also supported by a comparison of the structure models with periodic sequences AA and AB. We calculated no significant deviation of the interatomic distances of both models, which would result in a misfit between the differently arranged lamellas.

Observations of other zone axes with c^* perpendicular to the electron beam, e.g., $[\bar{1}30]$, underline the compatibility of the lamellas to different packings. The image simulations inserted in the micrograph of Fig. 4 was calculated on the basis of a supercell with quadrupled c-axis (space group $P1$) referring to the unit cell of the monoclinic $TlGaSe_2$-type structure. The sequence of consecutive lamellas was chosen to be ABAA. Black contrasts form squares which are connected by opposite edges to rows in the centers of the lamellas. These contrasts correlate with the projected potential of the potassium and indium atoms highlighted in the projection of the structure, see Fig. 4, right. The sequence of the lamellas within the supercell is unambiguously visible by the shifts of the structure along [001]. These shifts can also be recognized when following the line indicating [001] in the experimental image and in the simulated one. The rows of dark contrasts in the center of the lamellas again coincide along [001] for AA, but not for AB. As expected, there is no indication for a misfit between the differently stacked lamellas.

The pseudosymmetry of $KInS_2$ is an important prerequisite for the formation of polytypes without any significant change of the local structure at the boundaries. The polytypic structures are based on two shifts (vectors s_1 and s_2). As depicted in Fig. 5a, the two planes between a central layer and the adjacent layers are designated as boundary 1 and 2. In Fig. 5b the central layer is projected along [110] showing a pseudotranslation by the vector $s_1 = (1/4)a - (1/4)b$ for the sulfur atoms at boundary 1 (see marks). When rotating this layer around $[1\bar{1}4]$ by 90° (zone axis $[1\bar{1}0]$, Fig. 5c) it becomes clear that a pseudotranslation

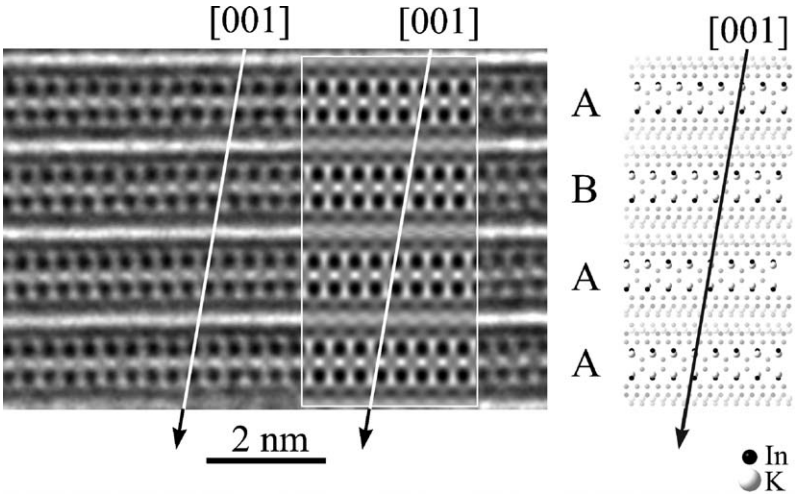

Fig. 4. HRTEM micrograph with $\Delta f = -35$ nm and inserted simulation (thickness: 3.5 nm). The simulation is based on the structure presented on the right side of the figure. The highlighted atoms correlate with dark contrasts forming squares in the micrograph.

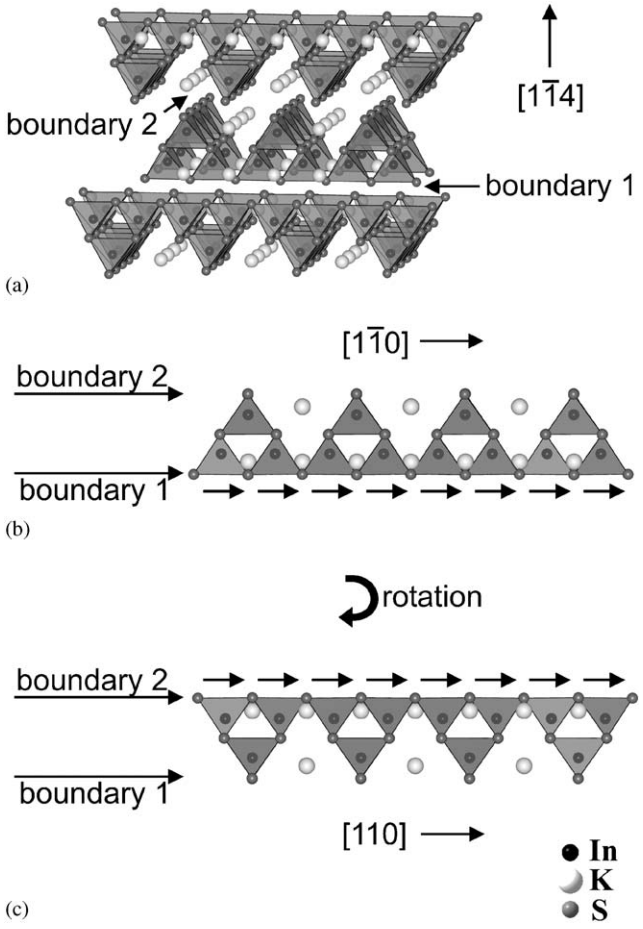

Fig. 5. Possible boundaries between ordered layers in the structure of $KInS_2$. (a) polyhedral representation, (b) projection of the central layer along [110], (c) projection of the central layer along [1$\bar{1}$0]).

perpendicular to the first one for the sulfur atoms at boundary 2 also exists, now by the vector $s_2 = (1/4)a + (1/4)b$. As depicted in Fig. 5a, the upper and lower edges of the InS_4 tetrahedra of adjacent layers are arranged in a way that they interlock like gear wheels in directions perpendicular to [1$\bar{1}$4]. An arrangement of the layers as observed in the orange modification of HgI_2 is not possible. This becomes evident when simulating a structure of $KInS_2$ with an arrangement of the layers as in HgI_2. In this case unfavorable distances of the sulfur atoms ($d = 2.51-2.57$ Å) between the layers occur. Hence, the basic arrangement of the layers as described by Eisenmann [9] is not violated even in the polytypic real structures. Therefore, the shifts s_1 and s_2 cannot be applied independently in neighboring layers. If for instance the central layer of Fig. 5a is shifted by the vector s_1, the adjacent layer connected with the central layer via boundary 2 is forced to be also shifted by s_1. When analyzing projections perpendicular to c the smallest discernible unit between two stacking faults is a lamella having a width of one unit cell (i.e., 14.76 Å) in the direction [1$\bar{1}$4]. This quantity should also determine the thickness of the separated plates depicted in Fig. 1 and therefore has large influence on the morphology of $KInS_2$.

Generally the sequence of the lamellas is random as depicted in the representative example of Fig. 6a. In rare cases extended domains characterized by ordered sequences in the given projection were observed, see the cut-out of an ordered region (sequence AABB) in Fig. 6b. In the case of ordered domains the diffuse scattering along c^* is resolved into sharp Bragg reflections. The enlarged section of the SAED pattern in Fig. 6c was taken for the zone axis [110] of a crystal with the sequence AAAAB, and the Bragg reflections $h\bar{h}l$ with $h = 2n+1$ clearly indicate the fivefold translational period of the structure along c^*. However, as HRTEM micrographs and SAED patterns are essentially projections, the ordering could be partially due to possible shifts perpendicular to the given

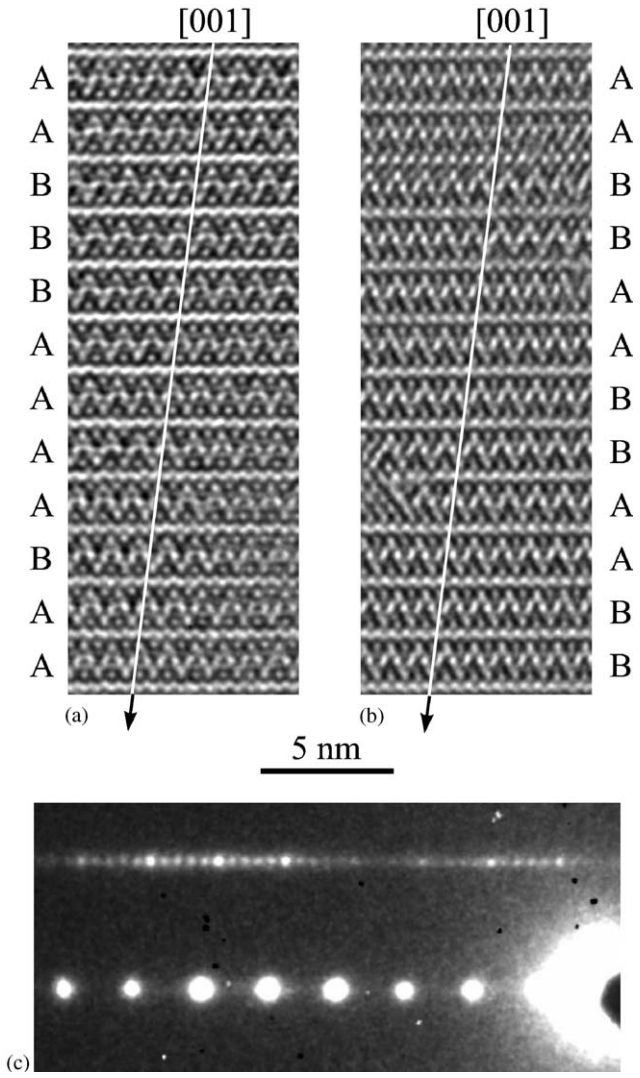

Fig. 6. (a) Disordered and (b) ordered stacking in the real structure of $KInS_2$, (c) cut-out of an SAED pattern of an ordered crystal with sequence AAAAB of consecutive lamellas.

projection. Hence, experimental limitations according to tilt does not allow to distinguish between the shifts s_1 and s_2 from projections only. The latter problem can be solved by a 3d analysis of reciprocal space (see next section). An interesting case of at least partial ordering is met for coexisting and extended domains with the sequences AA and AB. For the interpretation of the projection along [110] two models exist due to a close relationship between polytypic and twinned real structures. In Fig. 7a the sequence of the polytypic structure is AAAAABAB as shown by the arrow on the right side of the projection marking the direction [001]. On the left side of Fig. 7a an alternative interpretation is presented taking into account twinning. The twinning law[2] is a mirror plane (see horizontal arrow) perpendicular to $[1\bar{1}4]$ combined with a shift of $t = (1/8)a - (1/8)b$. Hence domain 1 is mirrored and c_1 of domain 1 switches to c_2 of domain 2. Both domains are characterized by the sequence AAAA within the twinned model of the real structure. The SAED pattern of Fig. 7b, left, was taken on a crystal with extended separated domains with sequences AA and AB, as checked by HRTEM and additionally by the calculation of Fouriertransforms (FFTs) of selected regions of the crystallite. They confirm that both FFTs are connected for instance via a mirror plane perpendicular to $[1\bar{1}4]$. The kinematical simulation of the diffraction pattern on the right side of Fig. 7b was calculated on the basis of a crystal with 2 domains. Each domain contains 16 lamellas having the sequences AA… and AB…, respectively. Referring to the above discussed twinning the twin ratio is fixed to 1:1. The convincing agreement between experimental and simulated pattern[3] and the $2mm$ symmetry of the pattern gives evidence for the close relationship between twinning and shifting in the real structure of $KInS_2$.

For the reasons discussed above electron microscopy is not sufficient for a full 3d analysis of the defect structure of $KInS_2$. However, the complementary use of XRD enables one to analyze the full reciprocal space and gives insight in the 3d distribution of the defects.

3.2. Simulation of diffuse X-ray scattering

In order to facilitate first simulations of the diffuse scattering, the structure of $KInS_2$ was transformed from the monoclinic $TlGaSe_2$-type structure to a rectangular cell. The transformation of the unit cell is described by the matrix P, the atomic coordinates in the new cell were calculated using the matrix Q (for the conventions of transformations see Ref. [16]

$$(a' \quad b' \quad c') = (a \quad b \quad c)P = (a \quad b \quad c)\begin{pmatrix} 1/2 & \overline{1/2} & \bar{1} \\ \overline{1/2} & \overline{1/2} & 0 \\ 0 & 0 & \bar{4} \end{pmatrix},$$

$$\begin{pmatrix} x' \\ y' \\ z' \end{pmatrix} = Q\begin{pmatrix} x \\ y \\ z \end{pmatrix} = \begin{pmatrix} 1 & \bar{1} & \overline{1/4} \\ \bar{1} & \bar{1} & 1/4 \\ 0 & 0 & \overline{1/4} \end{pmatrix}\begin{pmatrix} x \\ y \\ z \end{pmatrix}$$

with

$$|a'| \approx |b'| = \frac{|a|}{2}\sqrt{2} \quad \text{and} \quad |c'| = 4|c|\sin\beta.$$

The resulting unit cell consists of eight layers with identical arrangement of the layers to the one in the $TlGaSe_2$-type structure. The directions of the zone axes and the shifts by the vectors $s_1 = (1/4)a - (1/4)b$ and $s_2 = (1/4)a + (1/4)b$ can be transformed to $s_1' = (1/2)a'$ and $s_2' = (1/2)b'$ by using matrix Q. These

[2] A second description of the real structure is based on a rotation around $[1\bar{1}4]$ by 90°, i.e., domains in the zone axis orientation [110] intergrow with domains in the zone axis orientation $[1\bar{1}0]$.

[3] Besides the intensities of the reflections $h\,h\,l$ with $l = 4n$ which are strongly affected by multiple scattering.

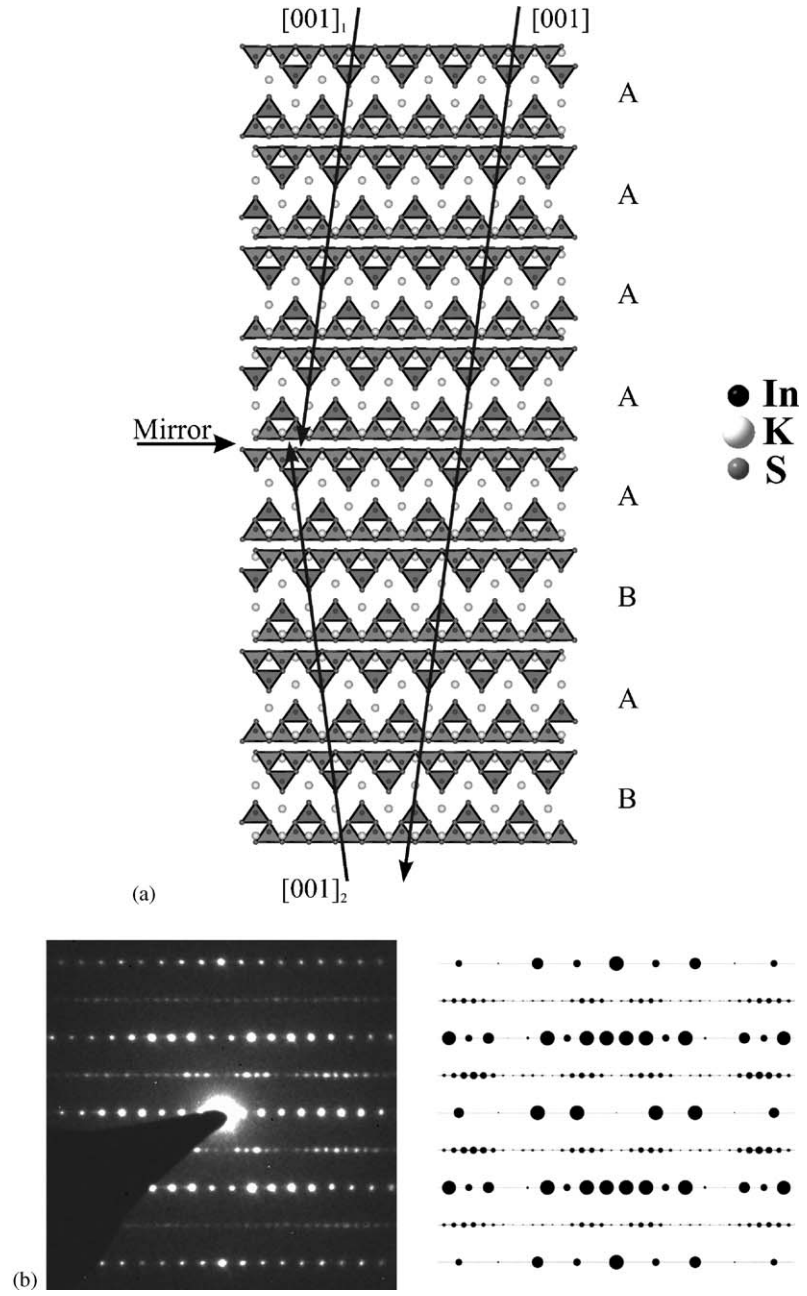

Fig. 7. Relation of twinned and polytypic structure in $KInS_2$. (a) Projection of a structure with sequence AAAAABAB of the lamellas (see arrows on the right side). Additionally the directions $[001]_{1,2}$ are marked on the left side which are connected via a mirror (see arrow) and a shift. (b) Left: experimental SAED pattern, right: kinematical simulation of the pattern based on a polytypic structure.

shifts are identical to the ones reported for the related, but essentially different real structure of the orange modification of HgI_2.

The perfect pseudotranslation of the sulfur atoms at the fault plane suggests a 1:1 ratio of shifted and non-shifted layers according to the $TlGaSe_2$-type structure. This ratio is a basic feature of an ordered supercell, which allows to approximate the diffuse X-ray scattering. Consequently, in the eight layer structure the first three layers were shifted by s_1', $s_1' + s_2'$ and s_2', see Fig. 8 for the projections along $b'(\cong[110])$ and $a'(\cong[1\bar{1}0])$. The resulting supercell contains four stacking faults between the eight layers, as indicated by the arrows in Fig 8. The observed Bragg reflections and the distribution of the diffuse intensities is well approximated by the calculated Bragg intensities based on the supercell, as depicted in Fig. 9 (left: simulation, right: experiment). As the diffuse streaks are extended along c^*, all layers

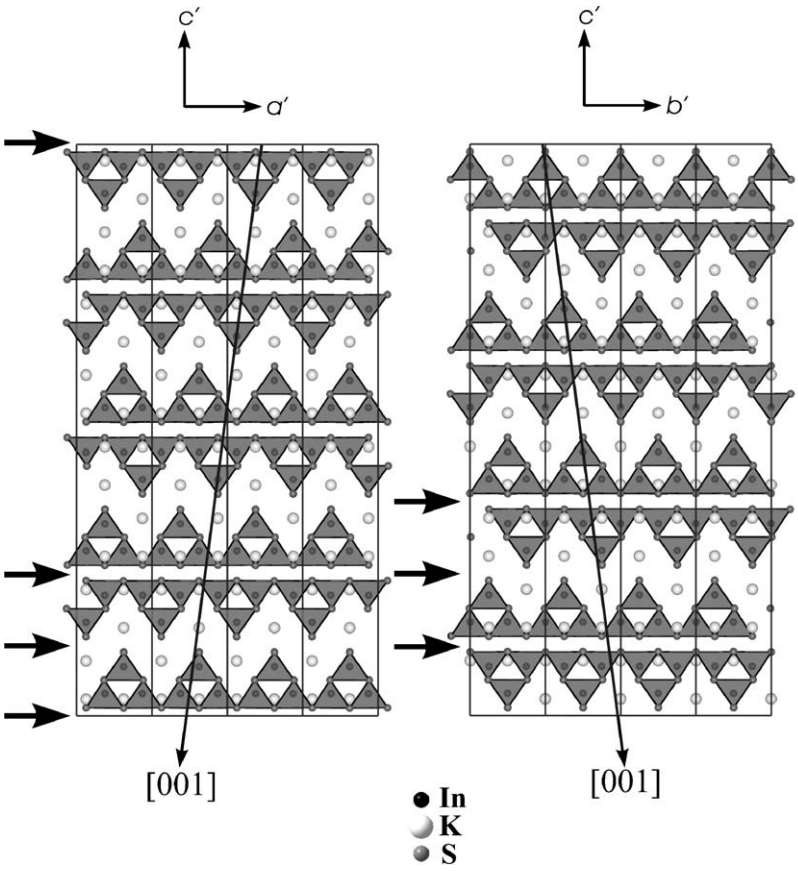

Fig. 8. Rectangular supercell for the approximation of the diffuse scattering by calculated Bragg intensities. Left: projected along b', right: projected along a'. The arrows mark the positions of fault planes.

perpendicular to [001] exhibit sharp reflections only, as shown in Fig. 9a for $h\,k\,2'$. The coexistence of Bragg reflections and diffuse intensities in the experimental pattern of $0\,k\,l'$ (Fig. 9b) is approximated well by the simulated one. All layers perpendicular to a' and b' are characterized by the same intensity distribution in the experimental and in the simulated patterns. This clearly indicates that the pseudotetragonal arrangement of the layers in the $TlGaSe_2$-type structure is not changed by the disorder, i.e., both possible shifts (s_1' and s_2') appear with equal frequency within the observed crystal. This is also confirmed by patterns containing diffuse scattering only, like every second layer of higher order Laue zones perpendicular to a' and b'. The convincing agreement between the experimental and simulated pattern of layer $h\,1\,l'$ is presented in Fig. 9c. The diffuse intensities are resolved into broad reflections with small reciprocal distances between them.

The program DISCUS [17] allows to calculate the diffuse component of the X-ray intensity. The simulations are based on the calculation of FFTs of entire crystals. In order to avoid contributions of finite size effects of the crystal to the simulated intensity, the average structure factor is subtracted. The basic crystals with sizes of $10 \times 10 \times 30$ unit cells (192,000 atoms) were modeled using the stack segment of DISCUS. The zero layers $h\,h\,l$[4] depicted in Fig. 10 were calculated using the lots-option[5] of DISCUS, applying periodic boundary options. The crystals possess different sequences of the lamellas with a varying degree of alternation with respect to A and B, see (a)–(c):

(a) sequence: AAABBBBBBAAAAAAABAAABAA-BBBAAAA
(b) sequence: AABBBABBBABAAAABBAABAAAB-BABBAA
(c) sequence: ABABABBABABABABABAAABAAB-BABABA

In case (a) the number of AB and BA neighbors is low. The crystal consists of larger domains with the same sequence, hence the diffuse intensities are concentrated on Bragg positions $h\,\bar{h}\,l$ forming diffuse

[4] The number of data points in the map was chosen $n(x) = 51$ and $n(y) = 51$; x-axis: 00l, y-axis: $h\,\bar{h}\,l$.

[5] One lot consists of a box with $10 \times 10 \times 5$ unit cells. The number of lots was 100.

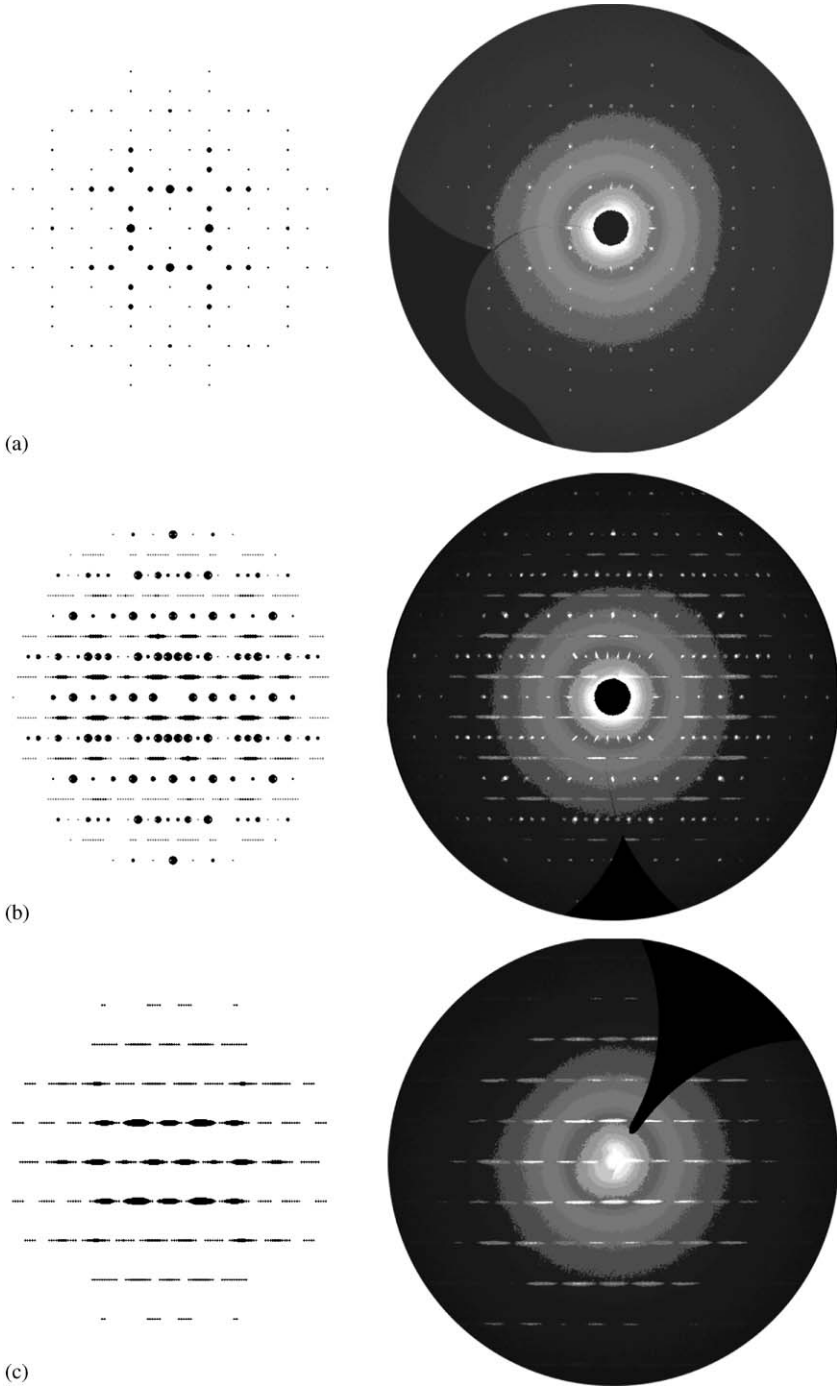

Fig. 9. XRD patterns of $KInS_2$, left: simulated patterns, right: experimental patterns. (a) layer $h\,k\,2'$, (b) layer $0\,k\,l'$ and (c) layer $h\,1\,l'$. The simulated patterns were calculated using the program WinGX 1.64.04 [18].

streaks along c^*. For (b) the number of AB and BA neighbors is increased. The diffuse intensities are split symmetrically around the positions of the Bragg intensities with $h\,\bar{h}\,l$. The crystal (c) is mainly characterized by the sequence AB or BA. Referring to zone axis [110], the diffuse intensities form streaks at the positions $h\,\bar{h}\,1/2$, see Fig. 10c.

Comparable variations in the distribution of the diffuse scattering were observed by SAED in small regions of the crystallites.

Besides these local variations, we also observed differences in the real structures when examining compounds isostructural to $KInS_2$. In the case of $RbInS_2$ highly ordered crystals can be prepared

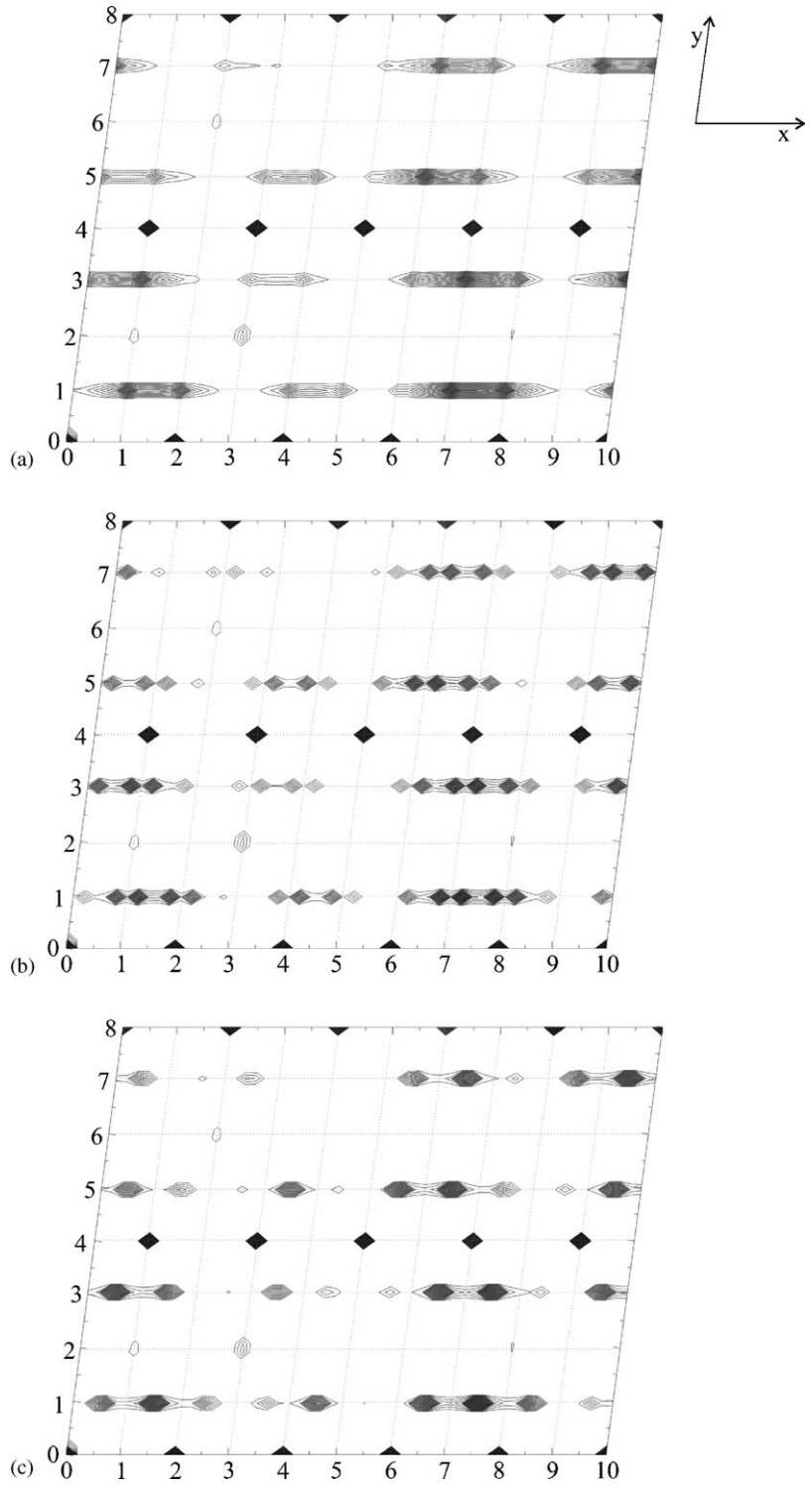

Fig. 10. Simulation of the diffuse scattering. The plots contain 5000 contour lines, starting from low Intensity ($I = 0$) with an increment of 0.02%. The displayed zero layer of $h\,h\,l$ was calculated for different sequences of the lamellas (a)–(c), see text. x-axis: $0\,0\,l$, y-axis: $h\,\bar{h}\,l$.

easily, according to our observations by XRD and HRTEM. The different real structures of the various isotypical compounds will be the subject of future investigations.

Acknowledgments

The authors thank Dr. C. Reiner, Prof. Dr. H. J. Deiseroth and Dr. K. Friese for helpful discussions.

References

[1] P. Villars, L.D. Calvert, Pearsons Handbook of Crystallographic Data for Intermetallic Phases, Vol. 1, ASM International, Metals Park, 1991.
[2] D. Müller, H. Hahn, Z. Anorg. Allg. Chem 438 (1978) 258.
[3] G.D. Guseinov, E. Mooser, E.M. Kerimova, R.S. Gamidov, I.V. Alekseev, M.Z. Ismailov, Phys. Stat. Sol. 34 (1969) 33.
[4] K.J. Range, G. Mahlberg, Z. Naturforsch. 30B (1–2) (1975) 81.
[5] H. Jansen, Dissertation, Universität Münster, 1985.
[6] D. Thiery, Dissertation, MPI Stuttgart und Universität Stuttgart, 1992.
[7] J. Weis, H. Schäfer, G. Schön, Z. Naturforsch. 31B (1976) 1336.
[8] C.K. Lowe-Ma, D.O. Kipp, T.A. Vanderah, J. Solid State Chem. 92 (1991) 520.
[9] B. Eisenmann, A. Hofmann, Z. Kristallogr. 195 (1991) 318.
[10] D.F. McMorrow, R.A. Cowley, P.D. Hatton, J. Banys, J. Phys.: Condens. Matter 2 (1990) 3699.
[11] D. Schwarzenbach, Z. Kristallogr. 128 (1969) 97.
[12] H. Jagodzinski, Acta Crystallogr. 7 (1954) 17.
[13] P.A. Stadelmann, Ultramicroscopy 21 (1987) 131.
[14] STOE & CIE, IPDS-Software, Version 2.93, Darmstadt, 1999.
[15] O. Jarchow, Fehlordnung, Polytypie und Untergruppenbeziehungen, Mineralog.-Petrogr. Institut, Universität Hamburg, 2001.
[16] T. Hahn (Ed) International Tables for Crystallography, Vol. A, Kluwer Academic Publishers, Dordrecht, Boston, London, 1993.
[17] Th. Proffen, R.B. Neder, J. Appl. Cryst. 30 (1997) 171.
[18] L.J. Farrugia, J. Appl. Cryst. 32 (1999) 837.